Current Topics in Biochemical Research
Vol. 22, 2021

Original Article

Spectroscopic and electrocatalytic studies on the reaction of NO_x with human serum albumin-heme complex

Mary Grace I. Galinato*,#, Ashley L. Lombardo, Emily M. Luteran, Robert S. Fogle III, Kevin S. Kang, Gary Fye, Amanda L. Dynoske and Jason A. Bennett*,$

School of Science, Penn State Behrend, Erie, PA, 16563, USA.

ABSTRACT

Heme enzymes catalyze the reduction of nitrite into different nitrogen-containing compounds *via* the nitrite reductase (NiR) mechanism. These systems contain a histidine, cysteine, or tyrosine residue proximal to the heme, with the latter system being less studied. This work focuses on the electrochemical reduction and spectroscopic studies of human serum albumin reconstituted with heme (HSA-heme), an artificial system that contains a weak Fe-O(tyrosine) interaction and demonstrates NiR activity. Cyclic voltammetry shows that HSA-heme in a surfactant film of dimethyldidodecylammonium bromide (ddab) behaves in a similar fashion to myoglobin/ddab. Both films exhibit fast electron transfer kinetics for the $Fe^{III/II}$ and $Fe^{II/I}$ redox couples as well as catalytic reduction of nitrite and nitric oxide (NO). In short, while both reduction processes suggest similar paths and products at HSA-heme, it was determined that NO initially binds to Fe^{III}, which is then chemically reduced to Fe^{II}, while nitrite binds to Fe^{II} after it is electrochemically reduced from Fe^{III}. This is similar to what is exhibited by myoglobin/ddab; however there appears to be some differences in the NO reduction mechanism between myoglobin and HSA-heme that is evident at faster scan rates. Importantly, the second-sphere coordination in HSA-heme (e.g. proximal ligand TYR161; and ILE142, LEU115, and TYR138 that display long- range interactions) plays an important role in NO_x electrocatalysis, as demonstrated through control experiments in the absence of the heme cofactor. Lastly, molecular docking studies demonstrate a slightly positive free binding energy of NO_x on both heme systems. This may be correlated with a lower nitrite formation constant and a faster reaction rate between nitrite and the heme center, as observed in previous studies.

KEYWORDS: (Human) serum albumin, heme, nitrite, nitric oxide, nitrite reductase, nitroxyl, electrochemistry, absorption and fluorescence spectroscopy, electrochemistry, molecular docking.

INTRODUCTION

Heme enzymes catalyze the reduction of NO_2^- to other nitrogen-containing compounds such as NO, N_2O, NH_3, and N_2. For example, assimilatory nitrite reductases (NiRs) convert nitrite to ammonia through a multielectron process (Eqn 1), while dissimilatory NiRs utilize several enzymes that transform nitrite to N_2 in conjunction with NO and N_2O reductases (Eqn 2).

$$NO_2^- \rightarrow NH_3 \quad (1)$$

$$NO_2^- \rightarrow NO \rightarrow N_2O \rightarrow N_2 \quad (2)$$

The reduction of NO_2^- to NO (Step 1, Eqn 2) is particularly interesting because it can be carried out by heme enzymes that have different ligands proximal to the cofactor, demonstrating the ability of organisms to utilize structurally diverse active sites for a common functionality. For example, the following heme enzymes listed along with their

*Corresponding authors
#galinato@psu.edu; $jbennett@psu.edu

proximal residue display NO_2^- to NO chemistry: myoglobin (Mb) [1-3] and hemoglobin (Hb) [4, 5] (histidine, His); *M. tuberculosis* CYP130 and CYP51 [6], and *S. solfataricus* CYP119 [7] (cysteine, Cys); and human serum albumin reconstituted with heme (HSA-heme) (tyrosine, Tyr) [8]. While more detailed studies on the NiR reaction have been carried out for the first two groups of hemoproteins enumerated above [1, 6, 9, 10], to our best knowledge, not much has been investigated for the latter. Here, we examine the NO_x reduction as catalyzed by HSA-heme, which contains a weak Fe-O(Tyr) binding interaction as described below.

HSA is the most abundant protein in plasma, and has a high-binding affinity for many molecules, including heme *b* ($K_A = 1.1 \times 10^8\ M^{-1}$) [11]. Heme *b* (or protoporphyrin IX) binds to HSA in a 1:1 ratio, forming a pentacoordinate complex with Tyr161 through its phenolate group approximately 2.7 Å away (Figure 1) [12]. Despite the rather long Fe^{III}-O_{Tyr161} distance, HSA-heme displays heme-based reactivity. For example, it exhibits peroxidase [13, 14] and weak catalase activity [14]. Also, variants of HSA reconstituted with Mn^{III} protoporphyrin-IX show superoxide dismutase activity [15]. Importantly, wild-type and engineered HSA-heme show thermodynamic and kinetic parameters for binding of diatomic ligands comparable to those of Hb and Mb [16, 17]. Unlike catalase (a hemoprotein with a Fe-O_{Tyr} bond) that has a low reduction potential (-426 mV vs SCE, pH 6) [18], the reduction potential of HSA-heme is significantly less negative (-200 mV vs Ag/AgCl, vide infra) and thus more amenable for NiR reaction studies that require the ferrous form of the complex.

This work utilizes spectroscopic studies and fluorimetric assays on the different forms of HSA-heme to elucidate the spectral features during NiR activity. Furthermore, electrocatalytic reduction of NO_x catalyzed by HSA-heme on surface-modified electrodes was conducted in order to understand this process through comparison with the more well-examined Mb system [7, 19, 20]. Lastly, molecular docking studies were performed in order to model the interaction of NO_x within the heme cavity of HSA-heme, with Mb as a reference for optimizing binding parameters. This allows us to understand key interactions between the ligand and nearby amino acids within the binding site, and how this might influence the NiR reaction.

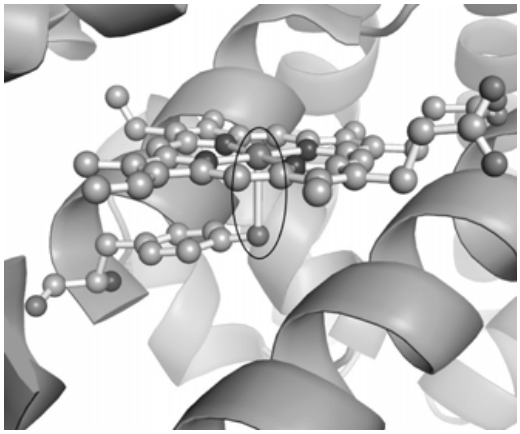

Figure 1. Crystal structure of human serum albumin, HSA-heme (PDB: 1N5U) [12]. The heme *b* cofactor and Tyr161 are presented as spheres, forming a weak Fe-O(Tyr161) interaction (encircled).

MATERIALS AND METHODS

Sample preparation

Human serum albumin was reconstituted with protoporphyrin IX according to a previous procedure [13]. Nitric oxide was scrubbed through KOH pellets to remove trace quantities of impurities. NO was bubbled into a previously degassed solution of 0.025 M phosphate/0.06M NaCl (pH 7.4) buffer to generate ~2 mM of a saturated solution of NO [21], which was used to make the Fe^{II}-NO complex for the spectroscopic measurements. Fe^{II} was prepared in the glove box by adding small amounts of sodium dithionite powder to Fe^{III} for the absorption studies and fluorimetric assays. Other chemicals such as 2,3-diaminonaphthalene (DAN) and standard 0.1 M nitrite solution were purchased from Sigma Aldrich.

The HSA-heme/ddab (dimethyldidodecyl-ammonium) and Mb/ddab electrode films were formed similar to that previously reported [7]. Simply, equal volumes of a 4.6 mg/mL ddab solution that was ultrasonicated for 5 h was mixed with a concentrated solution of the respective protein. Then 10 µL of the mixture was dropped onto a glassy carbon electrode that was previously polished with alumina slurries and electrochemically activated by cycling the potential in a 0.1 M KCl solution. The electrode was then allowed to dry overnight. For comparison, control electrodes were prepared in a similar manner and consisted of either a sole ddab, iron protoporphyrin IX (FePP)/ddab, or HSA (no heme)/ddab film.

Spectroscopic and electrochemical experiments

The NiR reaction for spectroscopic measurements was carried out by adding ~40 μL of an anaerobic 100 mM standard nitrite solution to ~600 μL of 3 μM Fe^{II} HSA-heme, and sealed in an airtight cuvette containing a microstir bar. The changes in the absorption spectrum of the protein were recorded on a Cary 60 spectrometer. The fluorimetric assay was carried out according to a previous method [22], and recorded on a Fluoromax-3 spectrofluorometer using a 335 nm excitation, and 4.0 nm emission and excitation slits.

All electrochemical experiments were carried out in N_2-saturated 0.1 M phosphate buffer solution (pH 7.4) containing 0.1 M KCl (KPi). The auxiliary electrode was a carbon rod and the reference electrode was Ag/AgCl (3 M NaCl). All potentials are referenced against this.

Molecular docking studies

The crystal structures of Mb and the NO_x ligands (PDB ID: 2FRK [23]), and HSA-heme (PDB ID: 1N5U [12]) were obtained from the Protein Data Bank. The receptor (protein) input files were prepared by first removing the water molecules and other unnecessary ligands or cofactors using a text editor. The ligand files (NO and NO_2^-) were prepared by taking their coordinates from the crystal structure of Mb-NO_x [23]. The files were then read in AutoDock Tools 1.5.7 to which atomic charges and hydrogens were added (where necessary) according to a protocol published by the authors of this software [24]. The correct charge to the metal center was manually added to the text file, as the software does not automatically incorporate this within its protocol. Molecular docking analyses were performed in AutoDock Vina within the suite of AutoDock Tools 1.5.7 [25], where the exhaustiveness was set to 24 as recommended by AutoDock Vina developers, the grid box parameters were set within the heme region, and the grid box spacing was set to 0.375 – 1 Å per grid unit for both receptors. A few trial simulations on HSA-heme were also set to 1.0 Å per grid unit.

RESULTS AND DISCUSSION

UV-vis and fluorescence spectroscopy

The spectral features associated with the relevant forms of HSA-heme (Fe^{II}, Fe^{III}, and Fe^{II}-NO) were generated and shown in Figure 2a. The Soret band of Fe^{II} occurs at lower energy (415 nm) than Fe^{III} (404 nm), which is consistent with previous work [13]. Distinct spectral features are also noticeable in the Q-region among the various HSA-heme species. For example, the bands at 503, 534, and 622 nm in Fe^{III} changes to a more pronounced two-peak feature at 536 and 572 nm upon reduction to Fe^{II}. Incorporation of NO to Fe^{II} generates the Fe^{II}-NO complex, and produces a Soret band at 401 nm which is characteristic of a pentacoordinate nitrosyl heme species, as previously reported [26]. This coordination is confirmed by EPR spectroscopy [27], suggesting that Tyr161 is not proximally ligated to the Fe center upon incorporation of NO, or is at least quite distanced for considerable interaction. In the Q-region, the distinct bands of Fe^{II} change to a subtle peak at 484 nm and broader features at 550 and 571 nm when the Fe^{II}-NO complex forms. The absorption spectrum of HSA-heme Fe^{II}-NO is similar to the five-coordinate NO adduct of ferrous soluble guanylate cyclase (sGC), which is characterized by a Soret band at 399 nm, a shoulder at 485 nm, and peaks at 537 and 572 nm [28]. Interestingly, a previous work reports that the Soret band of HSA-heme Fe^{II}-NO occurs at 389 nm [29], which is higher in energy than our observations. This may be due to the different experimental conditions or means of preparing the ferrous nitrosyl complex.

The NiR activity of HSA-heme was tested by adding NO_2^- to the Fe^{II} form and monitored *via* absorption spectroscopy. Dithionite was used to reduce Fe^{III} to Fe^{II} and was kept in slight excess to prevent its re-oxidation. Addition of NO_2^- to the faint yellow HSA-heme Fe^{II} solution shifts the Soret band from 415 nm to 401 nm (Figure 2b) producing a peach-colored solution. The observed trend in the shift of the Soret band (from low to high energy upon addition of NO_2^-) is consistent with Mb Fe^{II} [3]. In order to deduce the identity of the product, the absorption spectrum of Fe^{II}-NO was overlayed and normalized with the spectrum obtained from the reaction product of HSA-heme Fe^{II} and NO_2^-. As shown in Figure 2b, the features in both spectra match well, which suggest that HSA-heme Fe^{II} catalyzes the reduction of NO_2^- to NO. In both spectra, the Soret band occurs at 401 nm, while the Q-region displays a broad peak with a subtle shoulder at 571 and 550 nm, respectively,

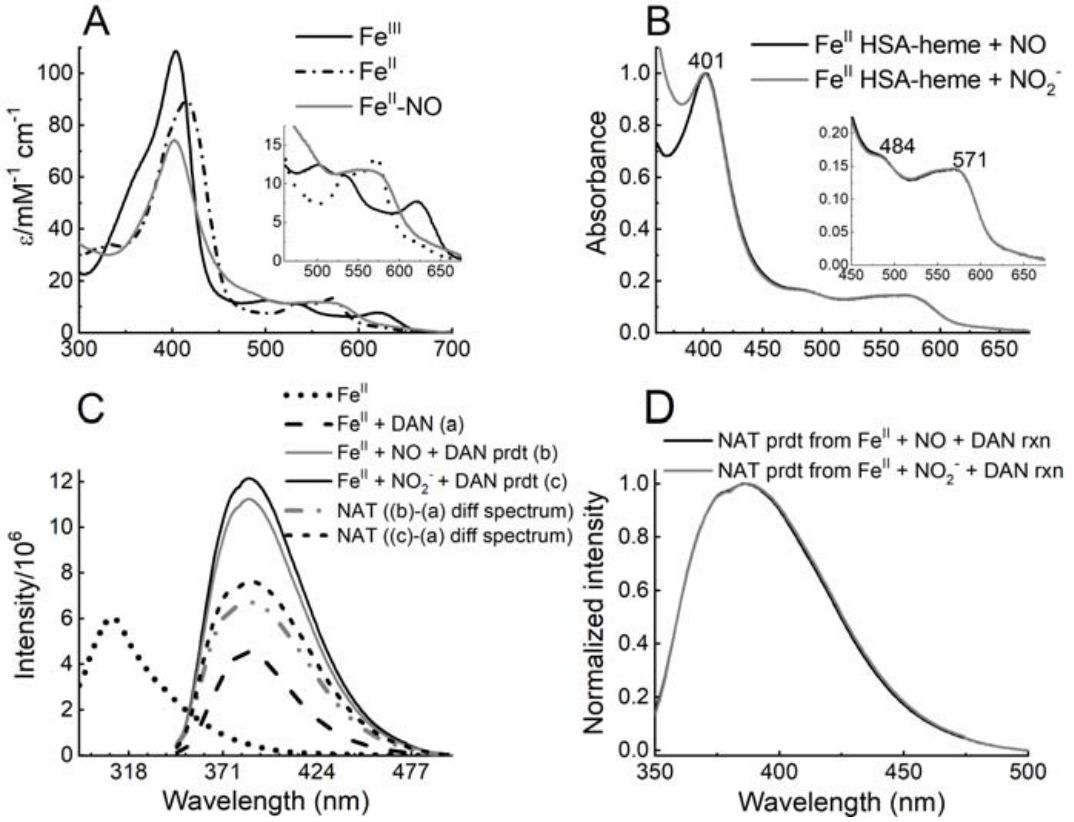

Figure 2. (A) UV-visible absorption spectra of Fe^{II}, Fe^{III}, and Fe^{II}-NO HSA-heme in 25 mM phosphate buffer with 60 mM NaCl, pH 7.4. (B) Overlay of the normalized absorption spectra of HSA-heme Fe^{II}-NO complex (black line) and the product of the reaction between Fe^{II} and NO_2^- (gray line). (C) Fluorescence spectra of Fe^{II}-HSA-heme and its corresponding reactions in the presence of NO_x and DAN. (D) Overlay of the normalized fluorescence spectra of NAT obtained from the reaction between DAN and HSA-heme Fe^{II}-NO (black line); and between the product of Fe^{II} and NO_2^- and DAN (gray line). Fluorescence spectra were recorded in 25 mM phosphate buffer with 60 mM NaCl, pH 7.4.

and a weak feature at 484 nm. Since dithionite is present in slight excess in solution, the final product is expected to only be Fe^{II}-NO. In globins, equimolar ratios of Fe^{II}-NO and Fe^{III} typically form when Fe^{II} and NO_2^- react [1, 3], however this is not the case in our NiR tests on HSA-heme Fe^{II}. Any Fe^{III} that may be generated during this reaction is immediately reduced to Fe^{II} by dithionite. Fe^{II} readily picks up NO that is produced during the NiR reaction and forms the stable Fe^{II}-NO complex, similar to that observed in globins [3, 5, 9].

Nitric oxide generated from the NiR reaction of HSA-heme Fe^{II} is further confirmed through a fluorimetric assay involving the N-nitrosation of 2,3-diaminonaphthalene (DAN). In the presence of NO_x species, DAN is converted to 2,3-naphthotriazole (NAT), which is a strongly fluorescent compound [22]. Importantly, DAN reacts only with NO under biologically relevant pH conditions (e.g. pH 7.4, at which our experiments were conducted) to generate NAT; at neutral pH, it remains relatively unreactive to NO_2^- [22]. This highly selective and sensitive fluorimetric assay can therefore probe NO production from the NiR chemistry of HSA-heme Fe^{II}. The emission spectrum of Fe^{II} shows a maximum at 309 nm that shifts to 385 nm in the presence of DAN (Figure 2c). In order to probe the spectral features associated with NAT formation under our experimental conditions, a saturated solution of NO was added to the solution of Fe^{II} and DAN. The intensity of the resulting fluorescence spectrum increased over two-fold, and the λ_{max} shifted slightly to lower energy

at 386 nm (Figure 2c). A similar assay was also conducted with Fe^{II} and DAN, but instead of adding NO, a solution of NO_2^- was added to test the NiR activity of HSA-heme. Figure 2d shows the spectral profile of pure NAT, which is achieved by taking the difference between the resulting product of combining Fe^{II} + DAN + and NO/NO_2^-, and that of Fe^{II} + DAN. An overlay of the two spectra indicates that the products from NO and NO_2^- reaction are very similar, thus confirming the NiR activity of HSA-heme.

Electrochemical catalysis

In order to better understand the NiR reaction of HSA-heme, the protein was first prepared in a surfactant film of dimethyldidodecylammonium bromide (ddab) on glassy carbon (GC). Its electrochemical property was then examined and compared to that of Mb (Mb/ddab), which has been thoroughly studied in the literature [7, 19, 20, 30, 31]. A water-insoluble surfactant film such as ddab is ideal for this study because it forms a stable, multilayer macrostructure that promotes rapid electrochemical response of redox active complexes (such as heme proteins) contained within it [30, 32].

Figure 3a compares the voltammetric i-E curves of the HSA-heme/ddab and Mb/ddab films in deaerated 0.1 M phosphate buffer solution (pH 7.4) containing 0.1 M KCl (KPi) at a scan rate of 2 V/s. Both films produce similar curves exhibiting two core reversible redox signals attributed to the $Fe^{III/II}$ (ca. -200 mV vs. Ag/AgCl) and $Fe^{II/I}$ (ca. -1080 mV vs. Ag/AgCl) redox couples, respectively. The HSA-heme/ddab film also exhibited a small reduction signal at -387 mV, which may be due to a small population of the heme occupying a

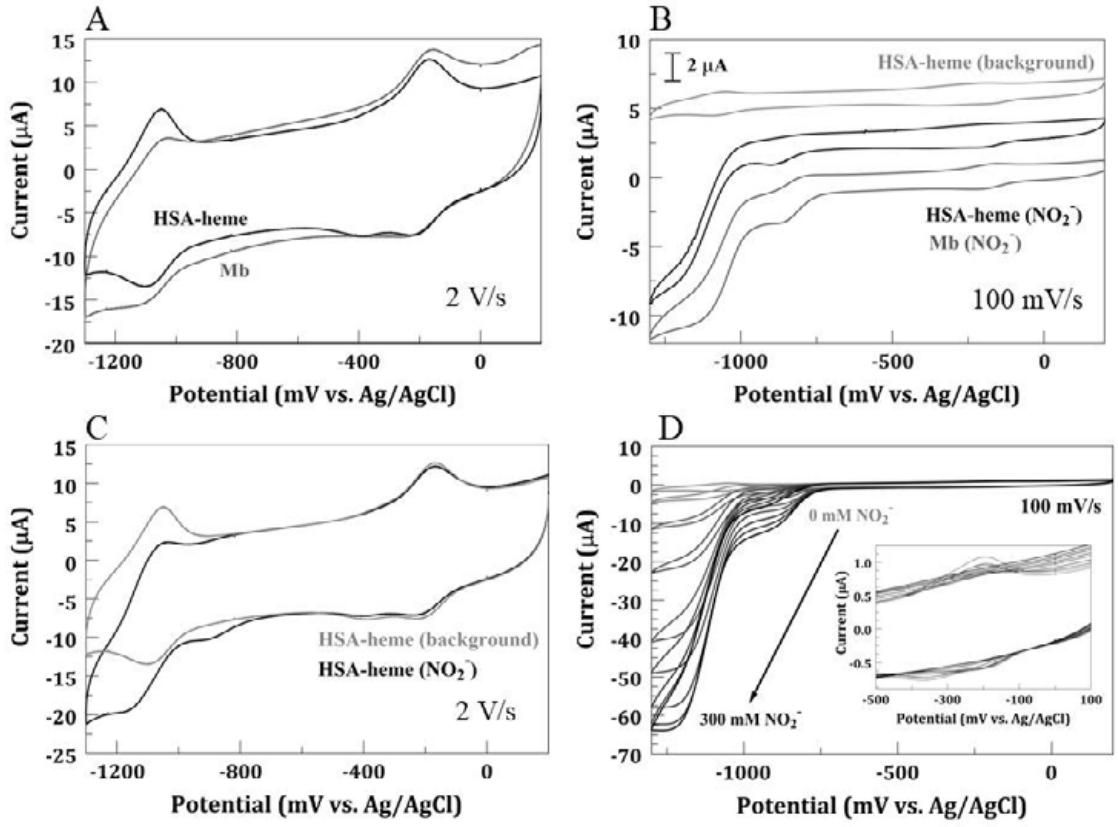

Figure 3. Voltammetric i-E curves of HSA-heme/ddab (black) and Mb/ddab (gray) films in N_2-saturated 0.1 M phosphate (KPi) solution with (A) 0 mM NO_2^- at 2 V/s, (B) 25 mM NO_2^- at 100 mV/s, and (C) 25 mM NO_2^- at 2 V/s. Figure 3D shows the change in the HSA-heme i-E curves with increasing NO_2^- concentration at 100 mV/s. The inset shows the region around the $Fe^{III/II}$ redox couple.

different pocket within the complex HSA matrix. Interestingly, there is only a minimal shift in the $Fe^{III/II}$ couple between the two films (-200 mV for Mb and -202 mV for HSA-heme); however there is a slightly larger cathodic shift of 15 mV in the $Fe^{II/I}$ couple for Mb compared to HSA-heme (-1091 vs. -1073 mV). These small differences are likely due to the different proximal environments and residues on the distal side of the heme within each protein.

In addition to the shifted reduction potential for the $Fe^{II/I}$ couple, the potential peak separation (ΔE_p) for this couple was only 46 mV at the HSA-heme film compared to the 118 mV exhibited by Mb. The ΔE_p for Mb was similar as that previously reported by Mimica *et al.* and suggests both rapid electron transfer and little reorganization of the molecules during the electron transfer process [33]. The significantly smaller ΔE_p exhibited by the HSA-heme, as well as the more symmetrical peak shape, not only suggests a fast electron transfer process, but also suggests that the HSA-heme behaves as an adsorbed thin-film with limited diffusion of charge carriers. It is important to note that while both protein/ddab films were physically stable for long periods of time, the Mb/ddab film remained electrochemically active for a much longer duration (e.g., 8 hr) compared to the HSA-heme/ddab film (e.g., 1 hr). Unlike Mb, the heme in artificial HSA-heme is loosely bound to its proximal ligand and held in place by non-covalent interactions within the protein, potentially making it less stable under the electrochemical conditions employed. Similar background voltametric i-E curves of control electrodes are shown in Figures S1 and S2 in the Supporting Information. Electrodes consisting of HSA (no heme)/ddab or ddab alone did not exhibit any heme redox peaks such as those seen in Figure 3. However, the electrode comprised of FePP/ddab did exhibit heme redox peaks. This supports that the peaks seen in Figure 3 are indeed due to the $Fe^{III/II}$ and $Fe^{II/I}$ redox couples. Additionally, a clean GC electrode in a solution of Mb did not show significant redox chemistry. This shows that the protein needs to be kept at the electrode surface *via* the ddab layer to achieve electron transfer.

Upon addition of 25 mM NO_2^- to the KPi solution, the voltammetric curves change considerably, providing information on the course of the reaction. Figure 3b compares the HSA-heme/ddab and Mb/ddab electrodes at a scan rate of 100 mV/s. For comparison, the background voltammetric i-E curve for the HSA-heme/ddab film at that scan rate is also shown. Both protein films exhibit comparable voltammetric characteristics upon introducing NO_2^-, including exhibiting the $Fe^{III/II}$ redox couple followed by two reduction signals; a pre-peak at ca. -900 mV (Mb = -884 mV, HSA-heme = -901 mV) as well as a large reduction signal at ca. -1200 mV. The large rise in current at potentials beyond -1000 mV in the presence of NO_2^- indicates catalytic turnover, where increasing number of electrons pass through the Fe heme site.

The similarity in the response of the Mb/ddab and HSA-heme/ddab films allows us to deduce several steps in the nitrite reduction mechanism. First, there is a small shift in the $Fe^{III/II}$ redox signal in the presence of NO_2^-. This is similar to that previously reported for Mb/ddab and hemoglobin/ddab (Hb/ddab) films and indicates an interaction between HSA-heme and NO_2^- [19, 33]. Interestingly, the spectral features of the Soret band for Fe^{III}-HSA-heme (404 nm) does not significantly change in the presence of small nitrite concentrations, however does show the formation of a peak at ca. 360 nm with increasing nitrite concentrations (not shown). In Mb, the binding constant of Fe^{III} with nitrite is fairly small (120 M^{-1}) indicating a weakly bound ligand to the iron center [3]. It would be reasonable to assume that HSA-heme would also likely exhibit weak binding for NO_2^-. This could explain the shift in the $Fe^{III/II}$ reduction as opposed to the complete disappearance of it. As the potential is scanned further negative, the voltammogram does not exhibit the $Fe^{II/I}$ redox couple. This is consistent with the Fe^{II} center complexing with NO_2^- and suggests that the reduction signals at ca. -900 mV and -1200 mV are due to NO_2^- reduction and not reduction at the ferrous center. These two reduction signals are consistent with previous work on Mb that displayed catalytic waves at -895 mV and -1205 mV (vs SCE), and were attributed to the reduction of a ferrous nitrosyl adduct (Fe^{II}-NO) and the subsequent generation of several gases, respectively [19]. Employing bulk electrolysis at -1205 mV, Farmer and coworkers showed the formation of NH_4^+ and NH_3OH^+ in the electrolysis solution after 2 hours [19]. In addition, analysis of

the head gas over bulk electrolysis using ^{15}N-labeled nitrite showed the presence of $^{15}N_2O$, $^{15}N_2$, and ^{15}NO after 5 minutes [19].

Figure 3c illustrates how the response of the HSA-heme/ddab film towards NO_2^- changes when the scan rate is increased to 2 V/s, with features substantially different from those in Figure 3b. As in Figure 3b, the $Fe^{III/II}$ couple is not significantly influenced by the added NO_2^-, and the reduction produces a pre-peak at -913 mV. However, unlike the curve at the slower scan rate, this curve exhibits the $Fe^{II/I}$ redox couple. This is consistent with the slow binding kinetics between NO_2^- and Fe^{II}-HSA-heme (1.3 M^{-1} s^{-1}) [8] and is similar to that previously reported for Mb/ddab films [33]. The influence of the heme center is highlighted by the absence of any significant reduction characteristics in the control electrodes, as shown in Figure S3. However, interestingly, the FePP/ddab film showed similar $Fe^{III/II}$ and $Fe^{II/I}$ redox signals to that of HSA-heme/ddab, along with a slight shoulder prior to the reduction of Fe^{II}. This likely suggests less interaction between NO_2^- and FePP compared to HSA-heme and NO_2^-, highlighting the importance of the protein matrix, particularly the amino acids in the second-sphere coordination that influences the thermodynamics of NO_x binding within the heme active site.

Figure 3d shows how the response of the HSA-heme/ddab film changes with increasing NO_2^- concentration (0, 10, 25, 50, 100, 150, 200, 250, and 300 mM NO_2^-). Upon introducing NO_2^-, the $Fe^{II/I}$ couple disappears and the current increases with NO_2^- concentration up to a limiting value of 250 mM. The shape of the curve and limiting concentration are consistent with reports on Mb/ddab that is characteristic of enzyme catalysis, and indicates catalytic turnover [19]. Additionally, while the $Fe^{III/II}$ redox couple was still evident in 25 mM NO_2^-, as the NO_2^- concentration is further increased, a decrease in this redox couple was observed (see inset) until it eventually disappeared. Mimica *et al*. suggested that this is indicative of nitrite binding at the Fe^{II}-heme site followed by a multielectronic reduction of the iron-nitrosyl intermediate [33].

Farmer and coworkers suggested that the reduction of nitrite at Mb resulted in the formation of a stable Fe^{II}-NO product as supported by our spectroscopic data above, which may then further get reduced to form Fe^{II}-NO^- [7]. Based on the similarity between the Mb/ddab and HSA-heme/ddab curves in Figure 3b, it appears that HSA-heme follows a similar mechanism for nitrite reduction of monomeric Mb [20].

In order to further understand the likely HSA-heme Fe^{II}-NO intermediate involved in NiR reactions, the reduction of 100 µM NO at HSA-heme/ddab was studied and compared against Mb/ddab at 100 mV/s and 2 V/s (Figures 4a and 4b). Both protein films show similar i-E curves in Figure 4a, most notably the absence of the $Fe^{III/II}$ redox couple and a large catalytic reduction peak at either -871 mV or -896 mV for Mb/ddab and HSA-heme/ddab, respectively. Farmer and co-workers explained this phenomenon on Mb/ddab electrodes as NO binding to the Fe^{III}, and chemically reducing to the Fe^{II}-NO species of the protein complex [34]. This species then undergoes reductive catalysis forming a ferrous nitroxyl species, Fe^{II}-NO^-. Bulk electrolysis of saturated NO solutions at -800 mV showed N_2O and NO_2^- formation [34].

Interestingly, once the scan rate is increased to 2 V/s (Figure 4b), the curves for HSA-heme/ddab and Mb/ddab are significantly different. For reference, the HSA-heme background curve is also shown in Figure 4b. There are two things worth noting. First, only Mb/ddab exhibits a small Fe^{III} to Fe^{II} reduction. This may suggest that the NO binds to the Fe^{III}-HSA-heme faster than to Mb on the time scale of the experiment. Second, while both proteins exhibit reduction of the Fe^{II}-NO complex at either -900 mV (Mb) or -936 mV (HSA-heme) (these reduction potentials fall within the range of previously reported values of NO adducts with Fe-porphyrin compounds [35-38]) followed by a second peak at -1127 mV (HSA-heme) or -1150 mV (Mb), respectively, the curves are significantly different on the reverse sweep. In the case of Mb/ddab, the reduction curves have previously been associated with the reduction of the Mb-Fe^{II}-NO complex followed by the dissociation of the nitroxyl ligand. This leaves the unligated Mb to exhibit the $Fe^{II/I}$ redox couple [34]. This would be consistent with the oxidation peak at -1027 mV exhibited by the Mb/ddab film (for the oxidation

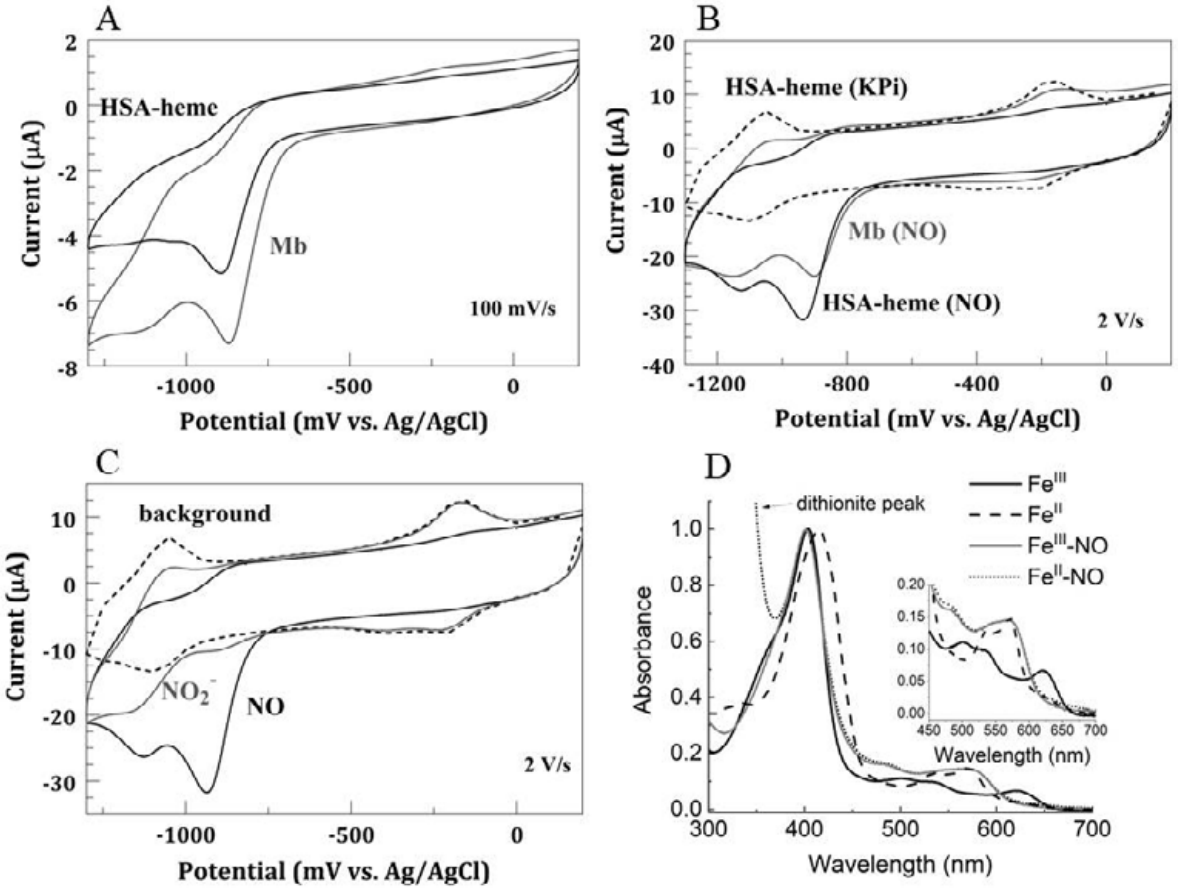

Figure 4. Voltammetric i-E curves of HSA-heme/ddab (black) and Mb/ddab (gray) in 100 μM NO at a scan rate of (A) 100 mV/s or (B) 2 V/s. Figure 4c is an overlay of the HSA-heme/ddab curves from 4b with that for 25 mM NO_2^- from Figure 3c. Figure 4d compares the UV-vis absorption spectra of Fe^{III} with (gray) and without (black) NO to that of Fe^{II} with NO after the Fe^{III} was reduced using dithionite (dotted lines) and without NO (dashed lines).

of Fe^{I} to Fe^{II}) as well as the emergence of the Fe^{II} to Fe^{III} oxidation at -145 mV. However, the HSA-heme film shows a very different response. In this case, the second reduction peak after the reduction of the HSA-Fe^{II}-NO complex is more complicated because it occurs at a less cathodic potential than that observed for the Mb film. This is in contradiction to the first reduction peak, which is at a comparatively more cathodic potential than observed for the Mb. Additionally, the forward sweep for the HSA-heme/ddab does not produce an oxidation peak. These characteristics are similar to that observed by Mimica *et al*. for NO reduction at Hb/ddab films and suggest that the reduction mechanism on HSA-heme is different to that at Mb [39]. Our results suggest a mechanism that needs further investigation but demonstrates that the NO is more readily released from the Mb than with HSA-heme. Unlike Mb that stays six-coordinate upon formation and subsequent reduction of the Fe^{II}-NO species due to the presence of the proximal His ligand [23, 40, 41], the Fe^{II}-NO complex in HSA-heme is five-coordinate [26] since the Tyr is relatively distant from the iron center. In Mb, the N-donor ligand (His) *trans* to NO "pushes" the spin density back from the iron center to the nitrosyl ligand, causing both the N-O and Fe-NO bonds to weaken [42, 43]. As a result, the nitrosyl ligand is more readily released from the iron center, as opposed to the case of HSA-heme. While little is known on the binding constant of NO to Fe^{II}-HSA-heme, the k_{off} of the dissociation of NO is low (1.7-8 x 10^{-5} s^{-1}) [26]. Further, in the case of ferric catalase, the binding

constant of NO is 8.7 x 10^6 M^{-1} [44]. These cumulative results suggest that the ferrous NO adduct of HSA-heme is stable. It is noteworthy that the binding constant of NO in ferrous Mb [45] is within the same magnitude as ferrous HSA-heme, but underscores the importance of the proximal ligand as well as nearby distal residues in controlling the reactions involving nitrosyl.

The response towards NO was further compared to the control electrodes, the results of which are shown in the Supporting Information. As expected, the HSA/ddab (no heme), Mb in solution, or the straight ddab electrodes did not show any reduction of NO in Figure S4 in agreement with their lack of heme redox signals. However, what was interesting was that the FePP/ddab electrode also failed to show any NO reduction characteristics in Figure S2, despite the heme redox properties. This film did show a decrease in the magnitude of both the $Fe^{III/II}$ and $Fe^{II/I}$ process, but only exhibited a significant shift in the peak potential for the former process. The reasons for this are unknown; however the fact that the response of this film is so different than those for Mb and HSA-heme shown in Figure 4b suggests that it is more than the mere presence of the heme center that gives these proteins NO reduction capabilities. For example, the interactions of the heme with the proximal ligand and the second-sphere amino acids (some of which are highlighted in the next section under Molecular Docking Studies) may influence this process.

Figure 4c overlays the voltammetric i-E curves for HSA-heme/ddab in KPi, 25 mM NO_2^-, and 100 µM NO at a rate of 2 V/s. It is apparent that the $Fe^{III/II}$ couple disappears in the NO solution, but not in the NO_2^- solution. This is consistent with NO binding to Fe^{III}, which is then chemically reduced to Fe^{II}-NO. To confirm this, Figure 4d compares the UV-vis absorption spectra of Fe^{III}, Fe^{II}, Fe^{III}-NO, and Fe^{II}-NO. The Fe^{II} and Fe^{II}-NO curves were generated by reducing the iron center with dithionite followed by the incorporation of NO. Most notable is the exact overlay of the Fe^{III}-NO and Fe^{II}-NO in both the Soret band at 401 nm and the Q-region at higher wavelengths (with the exception of the signal due to dithionite). This is consistent with NO binding to Fe^{III} and chemically reducing the complex to Fe^{II}-NO despite the absence of dithionite.

As the potential in Figure 4c is swept further negative, both NO and NO_2^- exhibit the same reduction potential of -936 mV, albeit the curve for NO has a much higher magnitude. This shows that both solutions result in the same HSA-heme Fe^{II}-NO complex. This is consistent with the absorbance spectra shown in Figure 2b (discussed above). Interestingly however, only the NO_2^- curve exhibits a $Fe^{II/I}$ oxidation at -1044 mV. As in Figure 3, this is likely due to the slow binding kinetics between NO_2^- and HSA-heme.

Overall, HSA-heme appears to follow similar mechanisms catalyzed by Mb. Based on the voltammetric and spectroscopic data and comparison with previous studies on Mb/ddab and Hb/ddab, a possible mechanism for the reduction of NO_2^- at HSA-heme can be suggested. First, the small shift in the $Fe^{III/II}$ redox couple (instead of complete disappearance) suggests that initial steps in the mechanism are the reduction of the heme followed by the binding of NO_2^- and likely reduction to the ferrous nitrosyl adduct as shown previously [7] and in reactions (3-5).

$$Fe^{III} + e^- \rightarrow Fe^{II} \quad (3)$$

$$Fe^{II} + NO_2^- + H^+ \rightarrow Fe^{III}\text{-}NO + OH^- \quad (4)$$

$$Fe^{III}\text{-}NO + e^- \rightarrow Fe^{II}\text{-}NO \quad (5)$$

After the initial reduction in the voltammogram, the similarities in the reduction signal at ca. -900 mV between Mb and HSA-heme, as well as comparing that for NO_2^- to NO scans, suggest that the next step in the mechanism is the reduction of Fe^{II}-NO as shown in equation (6).

$$Fe^{II}\text{-}NO + e^- \rightarrow Fe^{II}\text{-}NO^- \quad (6)$$

The formation of the Fe^{II}-NO species is supported through the absorption studies and fluorimetric assays described above.

The reduction mechanism for nitric oxide is slightly different between Mb and HSA-heme. Based on the disappearance of the $Fe^{III/II}$ redox signal and the similarities with that previously seen at very cathodic potentials for Hb/ddab films [39], a possible reduction mechanism for NO can be suggested as follows:

$$Fe^{III} + NO \rightarrow Fe^{III}\text{-}NO \quad (7)$$

$$Fe^{III}\text{-}NO + OH^- \rightarrow Fe^{II} + HNO_2 \quad (8)$$

$$Fe^{II} + NO \rightarrow Fe^{II}\text{-}NO \quad (9)$$

$$Fe^{II}\text{-}NO + e\text{-} \rightarrow Fe^{II}\text{-}NO^- \quad (10)$$

One major difference between HSA-heme and Mb is the lack of the $Fe^{III/II}$ redox couple and different voltammetric characteristics after eq. 10 (including the lack of $Fe^{II/I}$ redox couple) for HSA-heme at faster scan rates. While the exact reason for this is not fully known, this could suggest faster nitrosyl binding to Fe^{III}-HSA-heme on the time scale of the experiment compared to Mb, as well as HSA-heme not fully releasing the reduction products. It is also possible that HSA-heme follows a similar path as has been previously proposed for Hb/ddab in forming N_2O such as that shown by equations 11-13 [39]. This would explain the reduction at -1127 mV.

$$Fe^{II}\text{-}(NO^-) + NO \rightarrow Fe^{II}\text{-}(N_2O_2^-) \quad (11)$$

$$Fe^{II}\text{-}(N_2O_2^-) + e^- + 2H^+ \rightarrow Fe^{II} + H_2O + N_2O \quad (12)$$

$$Fe^{II} + e^- \rightarrow Fe^{I} \quad (13)$$

The fact that the reoxidation of Fe^I is not observed on the reverse scan may be explained by the interaction of Fe^I with the generated N_2O in the ddab film as suggested previously by Farmer [7] at CYP119 and shown in equation 14.

$$Fe^I + N_2O + H^+ \rightarrow Fe^{III} + N_2 + OH \quad (14)$$

The Fe^{III} could then bind to the excess NO in solution. Future experiments will focus on rotating disk experiments as well as head gas analysis in order to fully elucidate the complete reduction mechanism for both NO_x species at HSA-heme.

Molecular docking simulations

The parameters that were used to generate the Mb- and HSA-NO_x complexes with molecular docking were first tested by incorporating heme *b* into subdomain IB of HSA, where the cofactor is shown to bind within the protein scaffold [12]. In our simulations, the heme is buried in a pocket formed within the helices of the subdomain, forming a stable complex with HSA (-14.3 kJ/mol) through a weak coordination of the heme iron with the oxygen of Tyr161 located 2.71 Å away (not shown). This is analogous to the crystal structure of HSA-heme where the iron to oxygen distance is 2.73 Å. The orientation of the heme with HSA and the formation of a stable complex justify the accuracy of the parameters used for molecular docking simulations, at least within the system being investigated.

Several simulations on NO docking within the active site of Mb show an inverse trend between the Fe^{II}-NO bond length and free energy. Here, the conformations closest to the crystal structure demonstrate that as the bonding interaction between the heme iron and NO strengthens, the free energy becomes more positive: 2.883 Å and 0.4 kcal/mol; 2.517 Å and 1.3 kcal/mol; 2.272 Å and 2.3 kcal/mol. The latter simulation best predicted the Fe^{II}-NO bond length within the crystal structure of Mb (1.87 Å with the nitrite/dithionite method and 2.13 Å through the reaction of gaseous NO with Fe^{II}) [23]. Furthermore, the conformation of NO in the simulated studies is oriented differently, but not by much, from the crystal structure. The positive free energy observed in our work parallel a previous QM/MM study that shows a 1.82 kcal/mol free energy penalty for an alternative NO conformation relative to the crystal structure [46]. Our docking simulations were carried out using functions where the protein matrix and heme cofactor were set as rigid. This theoretical setup is different from an in *vivo* environment of crystallized proteins where the residues and heme have some flexibility. This may account for the discrepancy between the experimental and simulated results. Beyond the Fe^{II}-NO bond length, the predicted docking studies exhibit interactions between key residues within the distal pocket that are similar to those observed in the crystal structure, such as the H-bonding of NO to His64.

The best simulated configuration of Mb Fe^{III}-NO_2^- occurs when the ligand binds 2.024 Å away from the iron center *via* an O-atom (1.0 kcal/mol). This *O*-nitrito complex is also observed in the crystal structure of Mb, with an Fe-ONO^- bonding distance of 1.94 Å [23]. The ligand forms H-bonding interactions between the nitrite oxygen and the distal His64 stabilizing the complex, similar to that observed in the crystal structure. Interestingly, the *O*-bound form of nitrite in Mb is

not predicted to be the most stable isomer in density functional theory (DFT) calculations. For example, our prior DFT studies demonstrate the *N*-nitro complex to be ~4 kcal/mol more stable than the *O*-bound nitrite in Mb [3]. This trend is consistent with a prior work that shows the N-bound conformer of Mb Fe^{III}-NO_2^- to be more stable (by ~7 kcal/mol) than the *O*-nitrito complex [47]. Their work demonstrates a small increase in the spin density on the *O*-bound nitrito ligand compared to the *N*-bound form, but the difference is negligible to explain any differences in reactivities with other ligands (e.g. NO).

To our knowledge, no one has obtained the crystal structure of HSA-heme Fe^{II}-NO. Interestingly, the best score with about ~0.5 kcal/mol more stability than the next best predicted structure occurs when the oxygen in NO is closer to the iron center, which is not observed in the crystal structure of Mb/Hb or catalase Fe-NO. Catalase is a tetrameric enzyme containing a heme in each monomer, and a Tyr proximal to the iron center, similar to HSA-heme. Here, the following geometric features are observed, which are presented as an average of the four monomers: Fe-O(Tyr) distance of 1.98 Å; Fe-NO distance of 1.87 Å, tilt and bend angle of NO relative to the heme of 19° (consistent with *ferrous* Fe-NO complexes [44]), and the presence of a heme pocket water molecule 2.5 Å away from the oxygen of NO forming a strong H-bonding interaction [44]. Nearby residues in the distal pocket such as HIS74, PHE160, and ASN147 further stabilize the NO ligand. The conformation from the second highest scoring function of HSA-heme Fe^{II}-NO (3.3 kcal/mol) has features observed in catalase Fe-NO but with distances and tilt angles that are larger. For example, the Fe^{II}-NO distance is 2.60 Å, the NO tilt and bend angle is 64°, and the Fe-O(Tyr161) distance remains similar to that of the crystal structure at 2.73 Å (Figure 5a). Residues that show long range interactions with NO on the distal side include ILE142, LEU115, and TYR138 (Figure 5b). Here, ILE142 has the closest distance of 5.3 Å when measured from the oxygen of NO to the nitrogen of the N-terminal group of the residue. Two residues, His146 and Lys190, are closer to the carboxylic groups of the heme. In this simulation,

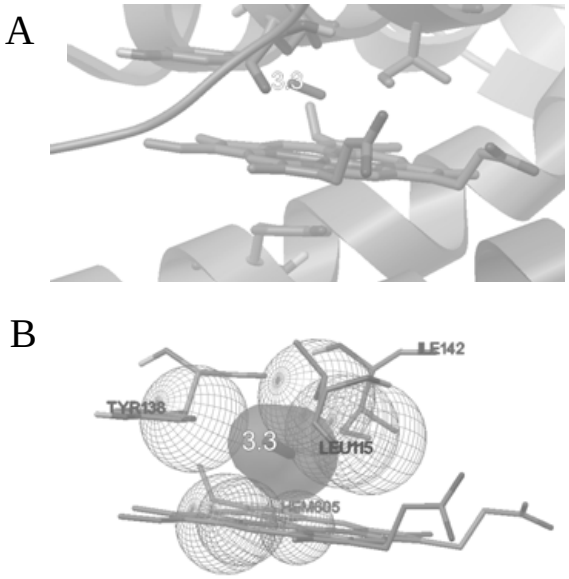

Figure 5. (A) Molecular docking simulations of NO to HSA-heme Fe^{II}. The label "3.3" on NO refers to the free energy (kcal/mol) of the Fe^{II}-NO complex. Tyr161 is shown on the proximal side of the heme opposite where NO is located. (B) Nearby residues on the distal side of the heme that interact with NO.

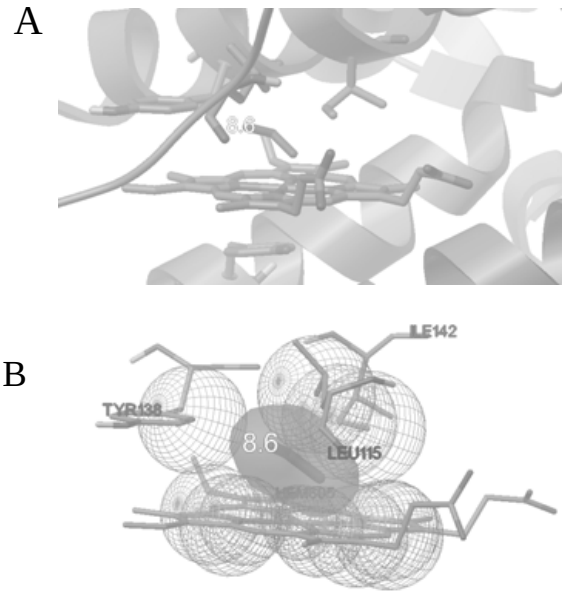

Figure 6. (A) Molecular docking simulations of NO_2^- to HSA-heme Fe^{II}. The label "8.6" on NO_2^- refers to the free energy (kcal/mol) of the Fe^{III}- NO_2^- complex. Tyr161 is shown on the proximal side of the heme opposite where NO is located. (B) Nearby residues on the distal side of the heme that interact with NO_2^-.

none of the residues were made flexible because doing so would completely shift them away from where they would typically be in the crystal structure. In reality, residues have some degree of flexibility, which may explain why the discrepancies observed in catalase Fe-NO in comparison to the corresponding complex in HSA-heme. Further, it is also noted that the water molecules in HSA-heme Fe^{II} were eliminated for ease in setting up the docking simulations. Water molecules near the heme may influence H-bonding interactions among residues and ligands.

The conformation generated from the best scoring function of nitrite to Fe^{III} HSA-heme bind *via* the oxygen in a fashion similar to a Mb *O*-nitrito complex [23], with a fairly high free energy of 8.6 kcal/mol. Here, the nitrite is located on the side of the heme opposite Tyr161, with an Fe^{III}-ONO^- bond distance of 1.80 Å, and a Fe-O(Tyr161) distance of 2.73 Å (Tyr was set as rigid, so the distance remains the same as in the crystal structure; see explanation above) (Figure 6a). Similar to HSA Fe^{II}-NO, long range interactions are observed among ILE142, LEU115, and TYR138, with the closest distance of 5.3 Å occurring from the non-bonded O of nitrite to the nitrogen of the N-terminal group of ILE142 (Figure 6b). The cumulative interactions of these three key residues may offset the positive free energy upon docking of nitrite close to the heme iron center. It is not unusual to observe changes in the binding energies of nitrite to the heme iron center with conformation. For example, the calculated binding energies of *N*-bound nitrite wild-type Mb was predicted at ~1.8 kcal/mol, but increased to a range of ~4.3-5.2 kcal/mol when nitrite was *O*-bound depending on the conformation [3]. It is important to note that these values were calculated *relative* to the most stable artificial Mb studied within reference [3]. In a previous study involving Mb, a high calculated binding energy correlated with a lower nitrite equilibrium constant ($K_{nitrite}$) and a faster reaction rate between nitrite and the heme center [3]. Given the parallel mechanisms observed in thereduction of nitrite catalyzed by Mb and HSA-heme (see discussion on electrochemical studies), the fairly high simulated free energy of nitrite binding to HSA-heme suggests that it supports a relatively fast reaction.

While the simulated free energies of NO_x bound close to the heme iron center generated positive values, we also obtained several scores with negative free energies (of around -1 to -3 kcal/mol) when the grid box was expanded. However, NO_x was nowhere near the iron center. Instead, the ligand formed H-bonding interactions with residues such as ARG117 or LEU182 in HSA-heme, which are both located further from the heme.

CONCLUSION

In summary, our results suggest different mechanisms of NO_2^-/NO reduction by HSA-heme despite both substrates forming a Fe^{II}-NO^- complex. In particular, the electrocatalytic reduction of NO by Mb and HSA-heme are quite different, highlighting the possible influence of the proximal ligand as well as nearby distal residues. These results therefore provide the initial groundwork for elucidating the effect of the heme proximal ligand (e.g. Tyr versus His) in producing NO under hypoxic conditions. Control experiments separately involving just heme and HSA demonstrate that the amino acid second-sphere coordination plays a crucial role in influencing the reduction of NO_x. While TYR161 (proximal side of heme) and ILE142, LEU115, and TYR138 (distal side of heme) are closest to the heme-bound NO_x and therefore most likely influence the thermodynamics and kinetics of binding, systematic point mutation investigations will definitively ascertain the exact residues involved. More studies will need to be carried out to pursue this idea.

ACKNOWLEDGEMENTS

R. S. F., A. L. L., G. F., and A. L. D. would like to thank Penn State Behrend Undergraduate Research Grant Programs for funding. M.G.I.G. thank the Spectroscopy Society of Pittsburgh for small equipment funding that was extended for use into research.

CONFLICT OF INTEREST STATEMENT

The authors declare no competing financial interest.

SUPPORTING INFORMATION

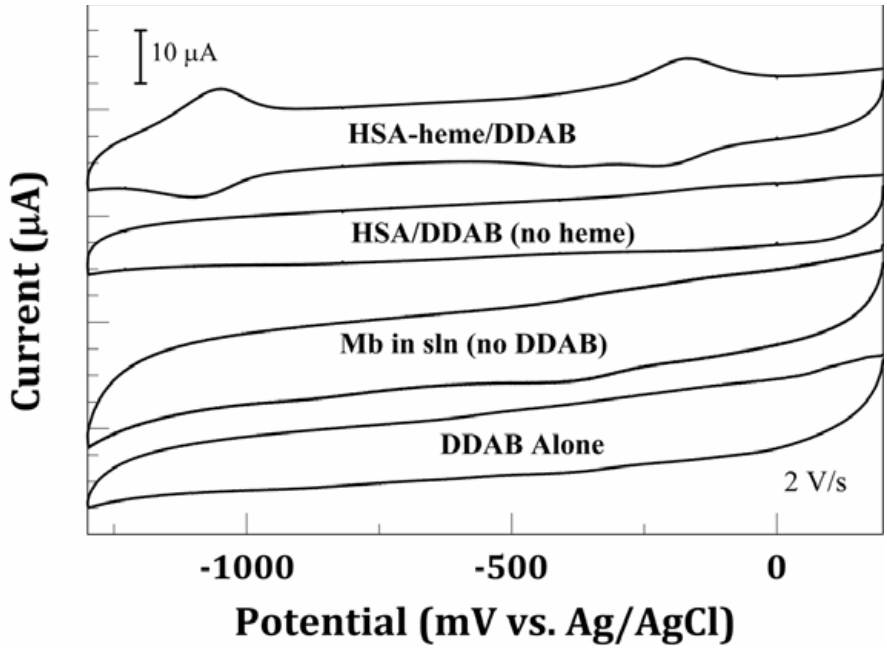

Figure S1. Voltammetric i-E curves of HSA-heme/ddab compared to control electrodes of HSA/ddab (no heme), clean GC in a Mb solution, and a ddab-modified electrode in N_2-saturated 0.1 M phosphate solution (KPi). Scan rate = 2 V/s.

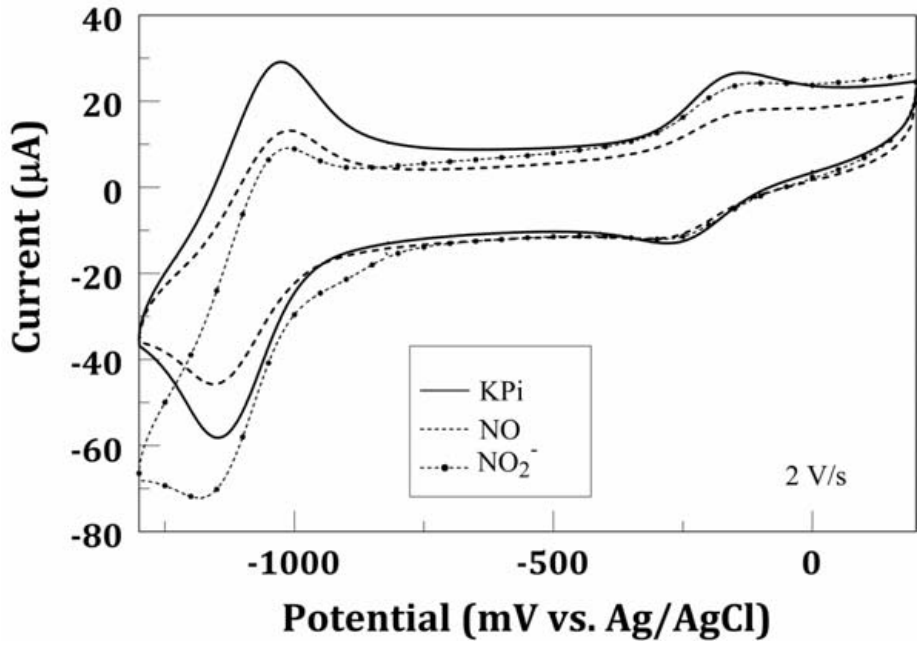

Figure S2. Voltammetric i-E curves of FePP/ddab electrodes in N_2-saturated KPi, 25 mM NO_2^- and 100 mM NO solution. Scan rate = 2 V/s.

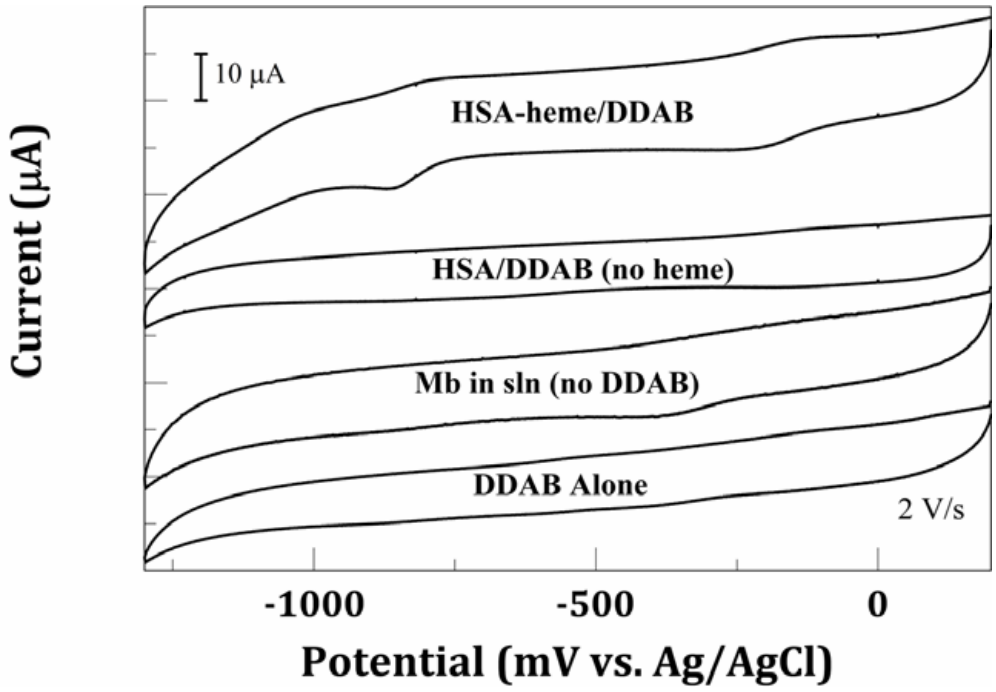

Figure S3. Voltammetric i-E curves of HSA-heme/ddab compared to control electrodes of HSA/ddab (no heme), clean GC in a Mb solution, and a ddab-modified electrode in 25 mM NO_2^- solution. Scan rate = 2 V/s.

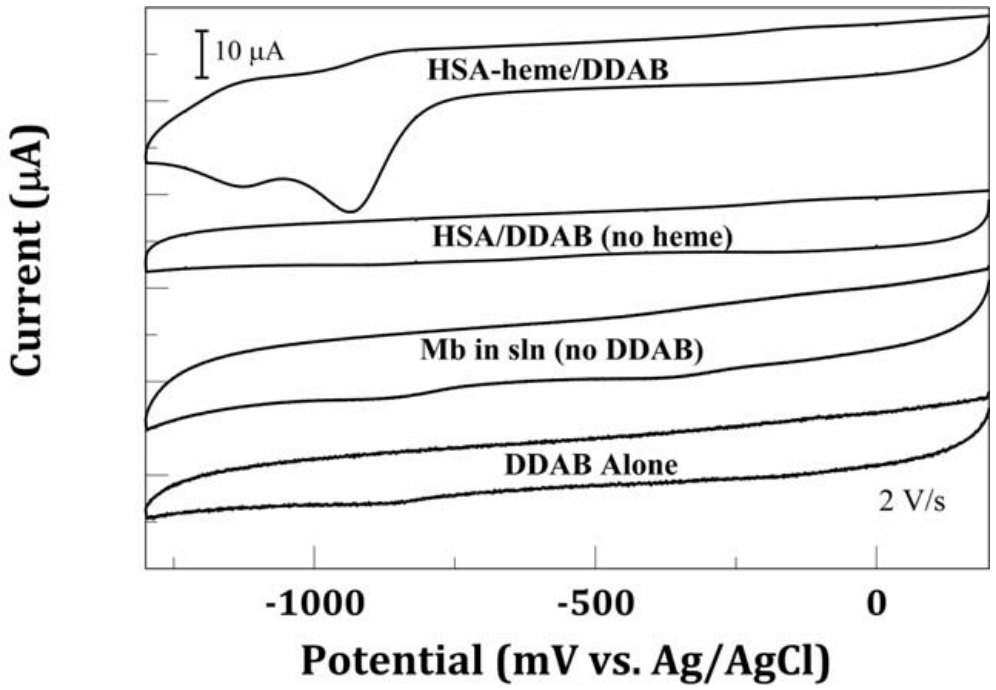

Figure S4. Voltammetric i-E curves of HSA-heme/ddab compared to control electrodes of HSA/ddab (no heme), clean GC in a Mb solution, and a ddab-modified electrode in 100 mM NO solution. Scan rate = 2 V/s.

REFERENCES

1. Shiva, S., Huang, Z., Grubina, R., Sun, J., Ringwood, L. A., MacArthur, P. H., Xu, X., Murphy, E., Darley-Usmar, V. M. and Gladwin, M. T. 2007, Circ. Res., 100, 654.
2. Yi, J., Heinecke, J., Tan, H., Ford, P. C. and Richter-Addo, G. B. 2009, J. Am. Chem. Soc., 131, 18119.
3. Galinato, M. G. I., Fogle, R. S. I., Stetz, A. and Galan, J. F. 2016, J. Inorg. Biochem., 154, 7.
4. Brooks, J. 1937, Proc. Royal Soc. London B. Biol. Sci., 123, 368.
5. Huang, K. T., Keszler, A., Patel, N., Patel, R. P., Gladwin, M. T., Kim-Shapiro, D. B. and Hogg, N. 2005, J. Biol. Chem., 280, 31126.
6. Ouellet, H., Lang, J., Couture, M. and Ortiz de Montellano, P. R. 2009, Biochem., 48, 863.
7. Immoos, C. E., Chou, J., Bayachou, M., Blair, E., Greaves, J. and Farmer, P. J. 2004, J. Am. Chem. Soc., 126, 4934.
8. Ascenzi, P., Tundo, G. R., Fanali, G., Coletta, M. and Fasano, M. 2013, J. Biol. Inorg. Chem., 18, 939.
9. Sturms, R., DiSpirito, A. A. and Hargrove, M. S. 2011, Biochem., 50, 3873.
10. Petersen, M. G., Dewilde, S. and Fago, A. 2008, Journal of Inorganic Biochemistry, 102, 1777.
11. Adams, P. A. and Berman, M. C. 1980, Biochem. J., 191, 95.
12. Wardell, M., Wang, Z., Ho, J. X., Robert, J., Ruker, F., Ruble, J. and Carter, D. C. 2002, Biochem. Biophys. Res. Comm., 291, 813.
13. Kamal, J. K. and Behere, D. V. 2002, J. Biol. Inorg. Chem., 7, 273.
14. Monzani, E., Bonafe, B., Fallarini, A., Redaelli, C., Casella, L., Minchiotti, L. and Galliano, M. 2001, Biochim. Biophys. Acta, 1547,
15. Kato, R., Kobayashi, Y., Akiyama, M. and Komatsu, T. 2013, Dalton Trans., 42, 15889.
16. Tsuchida, E., Komatsu, T., Matsukawa, Y., Nakagawa, A., Sakai, H., Kobayoshi, K. and Suematsu, M. 2003, J. Biomed. Mater. Res. A., 64, 257.
17. Komatsu, T., Ohmichi, N., Nakagawa, A., Zunszain, P. A., Curry, S. and Tsuchida, E. 2005, J. Am. Chem. Soc., 127, 15933.
18. Zhang, Z., Chouchane, S., Magliozzo, R. S. and Rusling, J. F. 2002, Anal. Chem., 74, 163.
19. Lin, R., Bayachou, M., Greaves, J. and Farmer, P. J. 1997, J. Am. Chem. Soc., 119, 12689.
20. Farmer, P. J., Lin, R. and Bayachou, M. 1998, Comments Inorg. Chem., 20, 101.
21. Hogg, N. and Kalyanaraman, B. 1998, In: M. A. Titheradge (Ed.) Nitric oxide protocols. Humana Press Inc. , Totowa, NJ, 231.
22. Miles, A. M., Wink, D. A., Cook, J. C. and Grisham, M. B. 1996, Methods of Enzymology. Academic Press, Inc., 105.
23. Copeland, D. M., Soares, A. S., West, A. H. and Richter-Addo, G. B. 2006, J. Inorg. Biochem., 100, 1413.
24. Morris, G. M., Huey, R., Lindstrom, W., Sanner, M. F., Belew, R. K., Goodsell, D. S. and Olson, A. J. 2009, J. Comp. Chem., 16, 2785.
25. Trott, O. and Olson, A. J. 2010, J. Comp. Chem., 31, 455.
26. Kharitonov, V. G., Sharma, V. S., Magde, D. and Koesling, D. 1997, Biochem., 36, 6814.
27. Fasano, M., Mattu, M., Coletta, M. and Ascenzi, P. 2002, J. Inorg. Biochem., 91, 487.
28. Stone, J. R. and Marletta, M. A. 1994, Biochem., 33, 5635.
29. Ascenzi, P. and Fasano, M. 2007, Biochem. Biophys. Res. Commun., 353, 469.
30. Rusling, J. F. and Nassar, A. E. F. 1993, J. Am. Chem. Soc., 115, 11891.
31. Ivanova, E. V. and Magner, E. 2005, Electrochem. Comm., 7, 323.
32. Nassar, A. E. F., Willis, W. S. and Rusling, J. F. 1995, Anal. Chem., 67, 2386.
33. Mimica, D., Zagal, J. H. and Bedioui, F. 2001, J. Electroanal. Chem., 497, 106.
34. Bayachou, M., Lin, R., Cho, W. and Farmer, P. J. 1998, J. Am. Chem. Soc., 120, 9888.
35. Olson, L. W., Schaeper, D., Lancon, D. and Kadish, K. M. 1982, J. Am. Chem. Soc., 104, 2042.
36. Lancon, D. and Kadish, K. M. 1983, J. Am. Chem. Soc., 105, 5610.
37. Barley, M. H. and Meyer, T. J. 1986, J. Am. Chem. Soc., 108, 5876.

38. Liu, Y., DeSilva, C. and Ryan, M. D. 1997, Inorg. Chim. Acta, 258, 247.
39. Mimica, D., Zagal, J. H. and Bedioui, F. 2001, Electrochem. Comm., 3, 435.
40. Brucker, E. A., Olson, J. S., Ikeda-Saito, M. and Phillips, G. N. J. 1998, Proteins: Struct. Funct. Genet., 30, 352.
41. Copeland, D. M., West, A. H. and Richter-Addo, G. B. 2003, Proteins: Struct. Funct. Genet., 53, 182.
42. Praneeth, V. K. K., Neese, F. and Lehnert, N. 2005, Inorg. Chem., 44, 2570.
43. Lehnert, N., Berto, T. C., Galinato, M. G. I. and Goodrich, L. E. 2010, In: K. Kadish, K. Smith and R. Guilard (Eds.) Porphyrin Handbook. World Scientific, Singapore, 1.
44. Purwar, N., McGarry, J. M., Kostera, J., Pacheco, A. A. and Schmidt, M. 2011, Biochem., 50, 4491.
45. Moore, E. G. and Gibson, Q. H. 1976, J. Biol. Chem., 251, 2788.
46. Wang, B., Shi, Y., Tejero, J., Powell, S. M., Thomas, L. M., Gladwin, M. T., Shiva, S., Zhang, Y. and Richter-Addo, G. B. 2018, Biochem., 57, 4788.
47. Basu, S., Grubina, R., Huang, J., Conradie, J., Huang, Z., Jeffers, A., Jiang, A., He, X., Azarov, I., Seibert, R., Mehta, A., Patel, R., King, S. B., Hogg, N., Ghosh, A., Gladwin, M. T. and Kim-Shapiro, D. B. 2007, Nat. Chem. Biol., 3, 785.